

An Overset Adaptive High-Order Approach for Blade-Resolved Wind Energy Applications

Andrew Kirby

Doctoral Candidate

University of Wyoming
Laramie, WY, USA

Michael Brazell

Postdoctoral Researcher

University of Wyoming
Laramie, WY, USA

Jay Sitaraman

Aerospace Engineer

Parallel Geometric Algorithms LLC
Sunnyvale, CA, USA

Dimitri Mavriplis

Professor

University of Wyoming
Laramie, WY, USA

ABSTRACT

An overset dual-mesh, dual-solver for computational fluid dynamics (CFD) is presented for wind energy applications. The dual-mesh paradigm is implemented in a near-body/off-body mesh system utilizing an unstructured mesh for the near-body and a Cartesian mesh for the off-body. The dual-solver paradigm uses variable-order, mixed-discretization solvers optimized for the respective near-body/off-body grids. Preliminary results of a computational study of the National Renewable Energy Laboratory (NREL) Phase VI wind turbine are presented. Results for uniform axial inflow velocities (7, 10, and 15 m/s) compare computed and measured results, including total power and thrust, sectional pressure coefficient, and a down-stream wake deficit profile for a uniform axial inflow velocity of 10 m/s. Qualitative results are presented for a dynamically mesh adaptive off-body solver in the dual-mesh, dual-solver paradigm. Preliminary results using a statically refined mesh indicate the power and thrust curves are over predicted and the pressure coefficient results indicate good agreement for the pressure side of the rotor blade but over prediction the suction side.

INTRODUCTION

With higher demand for wind energy, the wind industry has continually scaled its manufacturing capacity to new levels enabling lower-cost green energy. This movement requires the ability to more accurately predict large-scale wind energy production. Accurate prediction of reliability and efficiency is of critical importance, in particular for interactions between multiple wind turbines, since the upstream turbine wakes impact the efficiency of the downstream wind turbines.

Recent years have presented a developing field of research towards blade modelled simulation of wind turbines. Many previous works use finite-difference or finite-volume based discretizations (Refs. 1–14) to numerically model the fluid flow equations. The use of the finite element method has been demonstrated in a Arbitrary Lagrangian Eulerian Variational Multi-Scale (ALE-VMS) formulation showing good agreement in a validation study using the NREL Phase VI wind turbine (Ref. 15) including results using a fluid-structure interface (FSI). Additional studies using FSI models (Refs. 16, 17) have been investigated.

We present a dual-solver, dual-mesh overset framework which combines mixed-order CFD solvers. This dual-mesh system is framed into a near-body mesh and an off-body mesh similar to the CREATE-A/V HELIOS solver (Ref. 18). The solver used for the near-body mesh in this work, NSU3D, is the same near-body solver utilized in the HELIOS solver. However, we deploy a high-order discontinuous Galerkin fi-

nite element method solver for the off-body mesh in comparison to HELIOS which uses a finite-difference method. The use of a discontinuous Galerkin discretization offers advantages over traditional finite-difference or finite-volume discretizations in terms degree-of-freedoms being inherited by a single mesh element. The degrees-of-freedom in a mesh element are independent of other cells which in turn enables the use of coarser grids, thus minimizing the overheads associated with managing a dynamic adaptive mesh refinement process. Additionally, since the degrees-of-freedom of a cell are independent of neighboring cells, the use of variable spatial order solutions is possible. Through this approach, we aim to enable combined mesh refinement (h-refinement) and order enrichment (p-enrichment) adaptive methods, which have been shown to be optimal for error reduction (Refs. 19, 20). Additionally, the nearest neighbor stencil of the discontinuous Galerkin method simplifies the treatment of fringe data in transition regions between coarse and fine mesh interfaces.

The paper is outlined as follows. We first introduce the computational methodology deployed with the various solvers used in the dual-mesh, dual-solver framework. Next, we validate our computational methodology using the NREL Unsteady Aerodynamics Experiment Phase VI using a stand-alone turbine model without the tower or nacelle. An examination of the power and thrust curves for various uniform inflow velocities is presented, then an examination of the local behavior is performed through sectional performance of pressure coefficients, and lastly, down-stream wake deficits are examined. We conclude with a qualitative study using a dynamic adaptive mesh refinement solver used as the off-body mesh solver.

Presented at the AHS 72nd Annual Forum, West Palm Beach, Florida, May 17–19, 2016. Copyright © 2016 by the American Helicopter Society International, Inc. All rights reserved.

COMPUTATIONAL METHODOLOGY

This framework is known as the Wyoming Wind and Aerospace Applications Komputation Environment (W^2A^2KE3D). W^2A^2KE3D has been demonstrated on various aerospace applications such as a flow over a NACA0015 wing at moderate Reynolds number and flow over a sphere at low Reynolds number using a dynamically adaptive mesh environment (Ref. 21).

W^2A^2KE3D is framed in a near-body/off-body mesh system utilizing an unstructured mesh for the near-body mesh and a structured mesh for the off-body mesh as illustrated in Figure 1. The current framework allows for interchangeable solvers and mesh systems. Table 1 displays the solvers and their temporal discretizations. Table 2 displays the spatial discretization and mesh characteristics. Descriptions of the flow solvers are presented hereafter.

Table 1. W^2A^2KE3D Flow Solver Temporal Schemes

Solver	Temporal Discretizations
NSU3D (Ref. 22)	BDF2, BDF3
DG3D (Ref. 27)	BDF2, RK4
CartDG (Ref. 29)	RK2, RK4
SAMCartDG (Ref. 29)	RK2, RK4

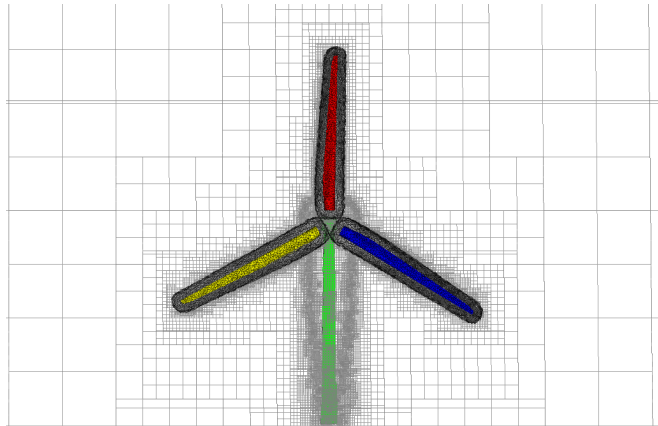


Fig. 1. Near-body/off-body mesh system utilized in the W^2A^2KE3D solver.

SOLVERS

Near-Body Unstructured Mesh Solver: NSU3D

The near-body unstructured mesh solver used in the present work is NSU3D (Refs. 22–24). NSU3D is a well-established vertex-centered finite-volume solver for mixed element unstructured meshes. NSU3D solves the Unsteady Reynolds Averaged Navier-Stokes (URANS) equations through a multi-grid technique. It has second-order spatial discretization using least-squares gradient reconstruction. NSU3D has second-

and third-order accurate temporal discretizations via the implicit BDF2 and BDF3 schemes, respectively. The solver has automatic agglomeration multigrid and line implicit preconditioning for solution acceleration. NSU3D has been thoroughly validated and verified through regular participation as a member of the AIAA High Lift Prediction Workshop (Ref. 25) and the AIAA Drag Prediction Workshop (Ref. 26).

Near-Body Unstructured Mesh Solver: DG3D

A second near-body unstructured solver in the W^2A^2KE3D solver collection is DG3D. DG3D is a high-order, mixed-and curved element unstructured mesh solver (Refs. 27, 28) capable of spatial order-of-accuracy ranging from first- to sixth-order. It is developed based on the discontinuous Galerkin (DG) finite element method (FEM) for the compressible Navier-Stokes equations. The temporal derivative is handled through an explicit Runge-Kutta method or an implicit BDF2 scheme. DG3D has been successfully applied to hypersonic problems, turbulent flow problems, full aircraft simulation, the Taylor-Green Vortex problem, and overset simulations (Ref. 21).

Off-Body Static Structured Mesh Solver: CartDG

CartDG is a high-order block Cartesian discontinuous Galerkin finite element method based compressible Navier-Stokes solver (Ref. 29). CartDG is a nodal, collocated, tensor-product basis formulation. It is developed to handle an arbitrary spatial order-of-accuracy and has explicit time-stepping of second- and fourth-orders via the Runge-Kutta method. CartDG in stand-alone mode has been demonstrated for various viscous and inviscid problems, notably the Taylor-Green Vortex problem (Refs. 30, 31) and the diagonally lid-driven cavity problem (Ref. 32).

Off-Body Structured AMR Solver: SAMCartDG

The off-body adaptive structured mesh solver SAMCartDG is the adaptive mesh refinement (AMR) extension of the CartDG solver. SAMCartDG is implemented into the Structured Adaptive Mesh Refinement Applications Interface (Refs. 34, 35) (SAMRAI) developed at Lawrence Livermore National Laboratory. SAMRAI is a patch based AMR system of properly nested refinement levels containing logically rectangular grid blocks. Grid generation and structure, parallel communication, and load balancing of SAMCartDG are handled by the SAMRAI infrastructure. SAMRAI allows for redistribution of restart solutions through file I/O. As a solution evolves over time, more features may need to be tracked increasing the number of elements in the solution. Between restart intervals of solutions, SAMCartDG is able to redistribute its solution to a different number of processors if needed. On regridding intervals, cells are tagged for refinement using feature-based detection. Tagging algorithms in SAMCartDG are based on density gradient, vorticity magnitude, and non-dimensional Q-Criterion (Ref. 36).

Table 2. W²A²KE3D Flow Solvers

Solver	Spatial Discretization	Spatial Order	Mesh	Mesh Movement	AMR	Spatial Order Adaption
NSU3D	FV	2	Unstructured	✓		
DG3D	DG FEM	1 – 6	Unstructured	✓	✓	✓
CartDG	DG FEM	1 – 12, 16, 32	Structured			
SAMCartDG	DG FEM	1 – 12, 16, 32	Structured	✓		

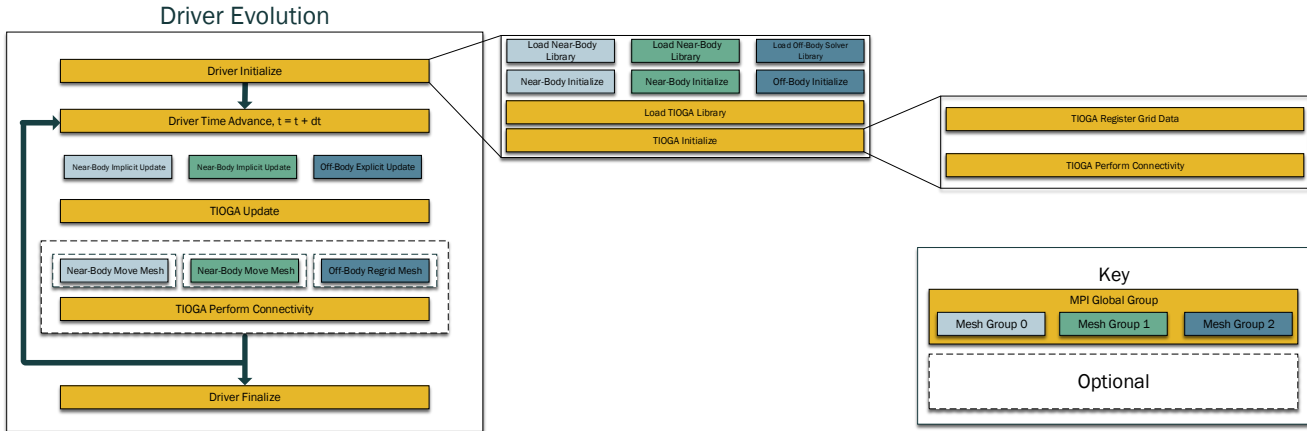


Fig. 2. Sample driver function used to choreograph multiple solvers and meshes with mesh movement and adaptation.

Overset Mesh Assembler: TIOGA

The domain connectivity and solution interpolation between the near-body and off-body meshes is handled by the Topology Independent Overset Grid Assembler (Refs. 37, 38) (TIOGA). TIOGA allows for parallel mesh interpolation between structured and unstructured meshes of variable spatial discretization order. The overset mesh assembler utilizes high-order interpolation to maintain overall high-order solution accuracy (Ref. 38). It has been demonstrated in mixed-order flow solver combinations for various problems such as the isentropic vortex (Ref. 38) and flow over a wing (Ref. 21).

Near-Body/Off-Body Mesh and Solution Choreography

In a multi-mesh, multi-solver paradigm, coordination of solvers is required. To choreograph the solvers, a C++ driver is implemented. Having multiple meshes and multiple flow solvers introduces variable amounts of computational work and computational intensity based on each flow solver which can lead to unbalanced resource utilization. To alleviate this problem, the driver allows for the near-body and off-body solvers to be executed on disjoint groups of processors. Additionally, at solution restart intervals, both NSU3D and SAMCartDG have the ability to redistribute their respective solutions to different numbers of processors independently allowing for more effective use of computational resources. An example driver is illustrated in Figure 2. For all simulations in the present work, the solvers advance their respective flow solutions for a predetermined characteristic time step. Once

each flow solver completes their time step, TIOGA interpolates the solution between the meshes, then the near-body mesh rotates an angle corresponding to the characteristic time step and the meshes are reconnected. For this work, we select the characteristic time step corresponding to 1° of rotation of the wind turbine blades.

RESULTS

NREL Unsteady Aerodynamics Experiment Phase VI

To evaluate the computational methodology presented in this work, a preliminary validation study is performed using the NREL Unsteady Aerodynamics Experiment Phase VI wind turbine (Refs. 39–42). The NREL Phase VI wind turbine is an experimental turbine that was tested at NASA Ames Research Center in the 80 ft x 120 ft (24.4 m x 36.6 m) wind tunnel. The experiment is regarded as one of the most extensive experimental studies performed for a wind turbine.

For this computational study, the blade radius is 5.029 m and the rotor is assumed to be rigid with the blade tip pitch angle of 3° and the yaw angle of 0°. The wind turbine is given a prescribed rotational speed of 72 revolutions per minute (rpm) which is performed by rotating the near-body unstructured mesh. The simulation structure contains only the rotor; no tower or nacelle is included in the simulation. Additionally, all simulations performed within the present work are time-dependent.

CREATE-A/V HELIOS Solver and FLOWYO Solver

In addition to experimental data comparison for the Phase VI wind turbine, we compare results with the CREATE-A/V HELIOS solver (Refs. 18, 43–45). HELIOS is an overset adaptive mesh solver for the Reynolds Averaged Navier-Stokes (RANS) equations. It uses NSU3D as the near-body solver and an adaptive fifth-order accurate finite-difference method with third-order accurate temporal discretization. HELIOS has been extensively validated using problems from aerospace such as forward-flight helicopters (Ref. 43) and from the wind energy field (Ref. 46). Specifically, we compare numerical results from Gundling et. al (Ref. 17). We note that the HELIOS solver performed steady, non-inertial simulations for the Phase VI wind turbine. The near-body and off-body meshes were connected one time through an overset process.

Further, we compare results to FLOWYO (Refs. 17, 47). FLOWYO is a RANS and Large Eddy Simulation (LES) solver.

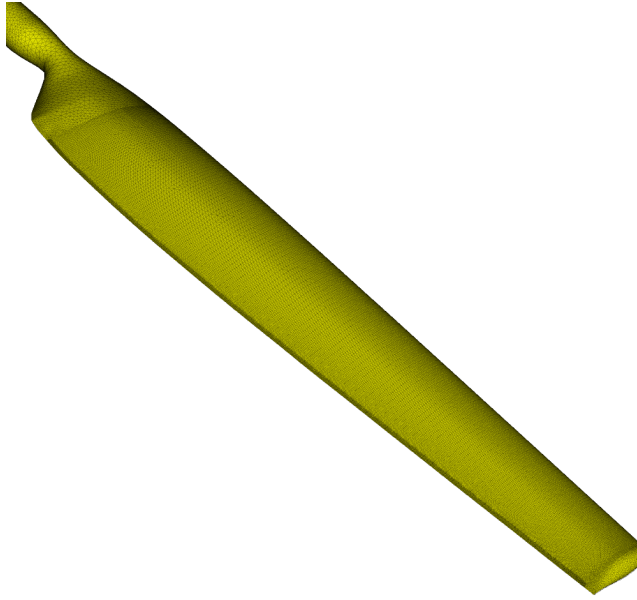


Fig. 3. Unstructured surface mesh of the NREL Phase VI wind turbine blade.

Near-Body Mesh and Solver Set-up

In all simulations performed, the near-body mesh in Figure 3 utilizes an unstructured mesh of approximately seven million cells and approximately three million nodes which extends approximately one chord length from the blade surface. A close-up of the blade tip of the Phase VI wind turbine is in Figure 4. The unstructured mesh contains both wind turbine blades.

The near-body flow and geometry characteristics are displayed in Table 3. We use NSU3D solver as the near-body solver. NSU3D is set to second-order spatial accuracy

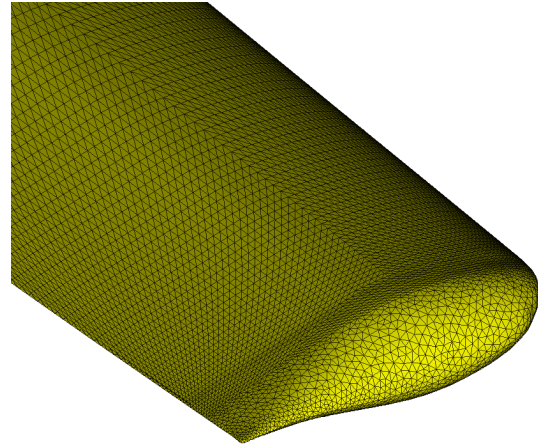


Fig. 4. Close-up of the unstructured surface mesh of the NREL Phase VI wind turbine blade.

and second-order temporal accuracy via the implicit BDF2 method. NSU3D completes 120 iterations to solve the characteristic time step and converges two orders of magnitude. The near-body solver calculations are performed in parallel on 256 processors.

Table 3. Near-body solver Phase VI parameters

Free-stream Inflow Velocity	M_∞
7 m/s	0.0206
10 m/s	0.0294
15 m/s	0.0441
Flow Solver Parameter	
Rotation Rate [rpm]	72
Rotation Rate [radians/sec]	7.540
c_∞ [m/s]	340.29
Tip Speed [m/s]	37.913
M_{tip}	0.1114
Reynolds Number	2,510,771
Blade Geometry	
Radius [m]	5.029
Tip Pitch Angle	3°
Yaw Angle	0°

Simulation Results

The first objective of this work is to validate the computed aerodynamic loads. Uniform axial inflow velocities of 7, 10, and 15 m/s are used for the power and thrust curve results. The outer computational domain is handled via the off-body mesh and connected through the overset assembler at locations where the near-body and off-body meshes overlap. For the power and thrust results, the off-body grid is com-

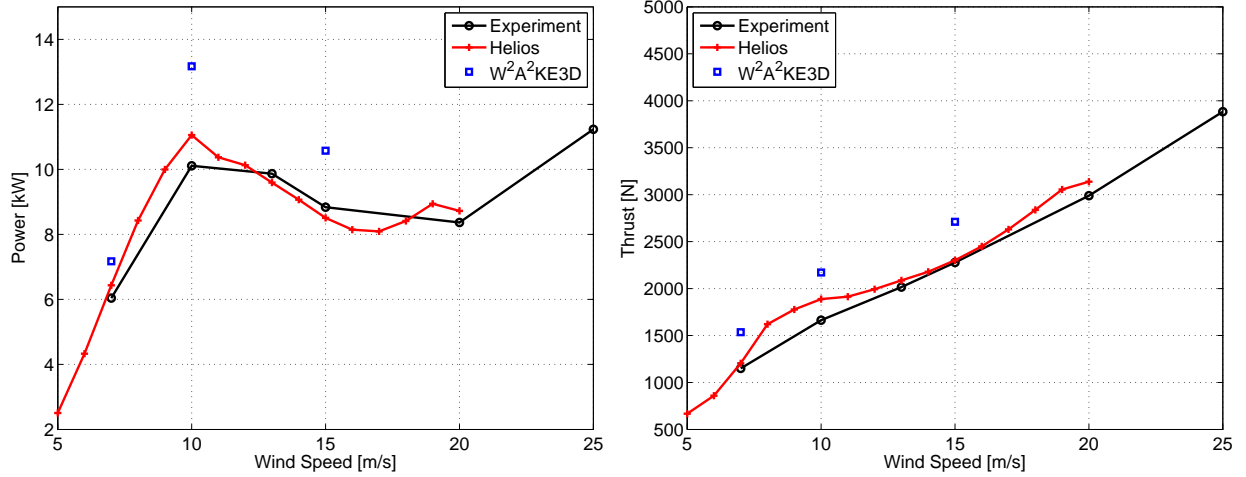


Fig. 5. Power and thrust curves for W^2A^2KE3D and HELIOS versus NREL experimental data.

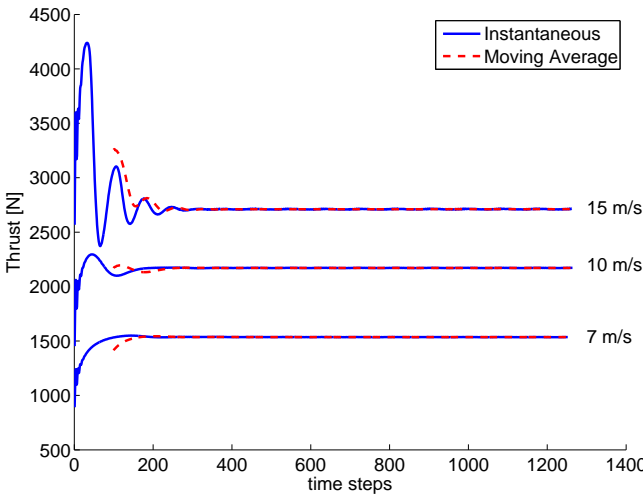


Fig. 6. Thrust convergence for inflow velocities 7, 10, and 15 m/s.

posed of a refined mesh of physical domain ($-7.5m, 7.5m$) \times ($-7.5m, 7.5m$) \times ($-3m, 27m$) using 192 elements in the x-direction, 192 elements in the y-direction, and 600 elements in the z-direction, respectively. The off-body solver is chosen to be CartDG which uses a second-order accurate spatial discretization of the inviscid Euler equations and a second-order accurate temporal discretization. We note the computational solution is time-dependent. At second-order spatial accuracy, the off-body solution contains approximately 177 million degrees-of-freedom (DOF) per equation which equates to approximately 885 million unknowns per Runge-Kutta stage. CartDG uses 8192 processors to solve the off-body calculations. The solvers are able to achieve approximately 1200° of rotation in a 12 hour compute window.

Power and thrust curves for W^2A^2KE3D and HELIOS are shown in Figure 5 along with the NREL experimental data. Thrust convergence history is displayed in Figure 6. The

power and thrust curves represent the integrated effect of the aerodynamic loads acting on the rotor blades. As indicated in Figure 6, convergence of aerodynamic loading is achieved for all the wind speeds. Larger number of time steps are required to obtain converged forces at higher wind speeds owing to the presence of flow separation.

To better examine the local behavior, we investigate the pressure coefficient over the blade surface at various sectional locations on the computational mesh used for the power and thrust curve analysis. The sectional pressure coefficient C_p is computed as

$$C_p = \frac{p - p_\infty}{\frac{1}{2} \rho_\infty (U_\infty^2 + (r\omega)^2)} \quad (1)$$

where U_∞ is the free-stream inflow speed, ω is the rotation speed, and r is the sectional radius. The off-body mesh is chosen to be the same as the mesh used in the power and thrust results. Figure 7 shows the surface coefficient of pressure at 10 m/s inflow velocity.

Figure 8 shows the pressure coefficient at 30%, 46.6%, 63.3%, 80% and 95% spanwise stations of the blade for 7, 10, and 15 m/s uniform inflow velocities. In all inflow velocity cases at all sectional locations, the coefficient of pressure values on the pressure side of the turbine blade are fairly well predicted. The S809 airfoil section used shows alleviation of the adverse pressure gradients at mid-chord regions, which manifests as an inflection in the pressure coefficient curves. The current analysis shows good agreement with data in prediction of this pattern. However, notice that in the 7 and 10 m/s cases, the coefficient of pressure on the suction side is higher than the experimental values at all sectional locations. Additionally, notable discrepancies are found at 10 m/s for the location $r/R = 46.6\%$, and for 15 m/s at $r/R = 30\%$. Similar inconsistencies are found in other researchers results (Refs. 4, 5, 13, 15) and is thought to be caused by inaccuracies in prediction of separated

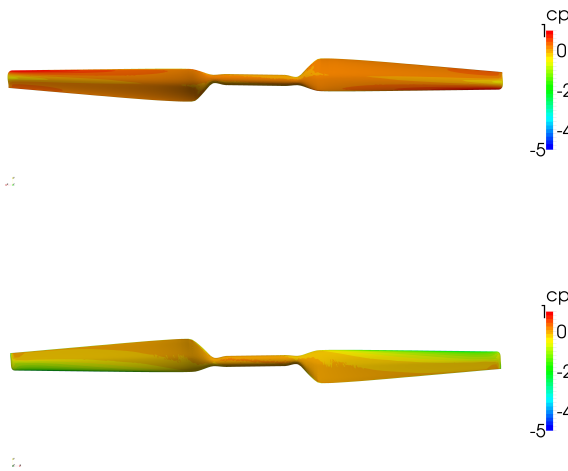


Fig. 7. Surface plots of the coefficient of pressure for inflow velocity of 10 m/s.

flow because of deficiencies in modeling laminar/turbulent transition.

A simulation is performed to analyze the wind wake velocity deficit. The computational domain is $(-11.25m, 11.25m) \times (-11.25m, 11.25m) \times (-5m, 55m)$ with 288 elements in the x-direction, 288 elements in the y-direction, and 1200 elements in the z-direction, respectively.

Figure 10 demonstrates the normalized wind velocity deficit along a line from the inlet of the domain to the outlet of the domain at a horizontal location of half a blade radius for inflow velocity of 10 m/s. Figure 11 demonstrates the normalized wind velocity wake deficits at 5 and 10 radius lengths downstream of the turbine blade. Notice the normalized velocity at the boundary interfaces in Figure 11; the values of the normalized velocity at the boundary interfaces should asymptote to a value of one representing free-stream. Typically an influence is observed when a computational domain is too small.

To compare the meshes used in the previous results, we increase the size and shift the computational domain to physical dimensions of $(-11.25m, 11.25m) \times (-11.25m, 11.25m) \times (-20m, 40m)$ with 288 elements in the x-direction, 288 elements in the y-direction, and 1200 elements in the z-direction, respectively. Notice the inlet boundary is now approximately four blade radius lengths away from the rotor blade. We list the mesh used in the previous results in Table 4 as Mesh-1 along side the larger, shifted computational mesh listed as Mesh-2. The larger computational domain increases the problem to nearly 800 million DOF per conservative variable for second-order spatial accuracy which equates to approximately 4 billion unknowns per Runge-Kutta stage. Approximately 1000° of rotation is achieved in a 12 hour simulation campaign. Figure 12 shows the inflow velocities coming inboard to the rotor blade. Notice that for the larger computational

domain, the inboard velocity is closer to the FLOWYO and HELIOS results. However, the inlet velocity hasn't dropped to the same velocity as the HELIOS results.

Table 4. Wake Deficit Profile Meshes

Domain	Mesh-1	Mesh-2
x_{lo}	-11.25	-11.25
x_{hi}	11.25	11.25
y_{lo}	-11.25	-11.25
y_{hi}	11.25	11.25
z_{lo}	-5.0	55.0
z_{hi}	-20.0	40.0
<hr/>		
Elements		
N_x	288	288
N_y	288	288
N_z	1200	1200

Figure 13 shows the pressure coefficients of the smaller domain compared to the pressure coefficients of the larger domain at a free-stream inflow velocity of 10 m/s. Results are slightly improved when using the larger computational domain for the suction side of the rotor blade. These slight improvements reflect the positive impact of using a larger computational domain.

Figure 14 illustrates the difference between the two meshes for the normalized wind velocity deficit profiles along a line from the inlet of the domain to the outlet of the domain at a horizontal location of half the blade radius for inflow velocity of 10 m/s. Figure 15 demonstrates the normalized wind velocity deficit comparison at five blade radius lengths downstream of the turbine blade. We see a significant improvement over the computational results of Mesh-1 by using Mesh-2. This confirms the hypothesis that the domain used in the initial results has the inlet boundary close to the rotor blade. Both of the present results give a higher wind speed velocity compared to the HELIOS numerical result. However, both W²A²KE3D results do give better solutions than the FLOWYO (Ref. 17) result. Notice the normalized velocity at the boundary interfaces in Figure 15; the values of the normalized velocity at the boundary interfaces should asymptote to a value of one representing free-stream.

DYNAMIC ADAPTIVE MESH RESULTS

Computations that use a moving near-body mesh system in an AMR hierarchy is an upcoming capability of W²A²KE3D infrastructure and only preliminary results are available at this time. The adaptive solution is computed using a computational domain of $(-49m, 49m) \times (-49m, 49m) \times (-50m, 202m)$. Figure 16 shows the adaptive mesh solution using approximately five million elements.

Further reduction in the total elements is obtained via an overset mesh resolution matching algorithm. The overset mesh assembler requires the near-body and off-body meshes be of the same approximate size in the overlap regions. To save elements in the off-body mesh, the mesh is adapted to

a set of outer boundary grid points provided by the trimmed near-body unstructured mesh. The geometric adaption of the off-body grid refines to a prescribed reference length provided for each near-body grid boundary point. Figure 16 shows the off-body mesh geometrically and solution adapted to the NREL Phase VI blade.

CONCLUSIONS

The methodology was evaluated using a full rotor model of NREL Unsteady Aerodynamics Experiment Phase VI. The performance measures of power and thrust curves were over predicted compared to the experimental data when using second-order accuracy in the near-body and off-body with a refined off-body mesh. Use of small and ill-placed computational domains significantly impacted the accuracy of the simulations. Using a larger domain that was shifted to allow for a greater distance between the inlet boundary and the rotor blade slightly improved the wake velocity deficit profile results.

Future work entails using the high-order adaptive off-body solver SAMCartDG at higher solution accuracies. Further development of the adaptive mesh solver is included in future work in addition to verification and validation. Numerical comparison with the HELIOS solver for adaptive results will also be conducted. The tower and nacelle will also be included into the Phase VI computational simulations for analysis of the wind speed deficits.

Author contact: Andrew Kirby, akirby@uwyo.edu

ACKNOWLEDGMENTS

This work was supported in part by ONR Grant N00014-14-1-0045 and by the U.S. Department of Energy, Office of Science, Basic Energy Sciences, under Award DE-SC0012671. Computer time was provided by the NCAR-Wyoming Supercomputing Center (NWSC) and University of Wyoming Advanced Research Computing Center (ARCC).

REFERENCES

- ¹Takizawa, K., Henicke, B., Tezduyar, T. E., Hsu, M.-C., and Bazilevs, Y., “Stabilized space–time computation of wind-turbine rotor aerodynamics,” *Computational Mechanics*, Vol. 48, (3), 2011, pp. 333–344.
- ²Bazilevs, Y., Hsu, M.-C., Akkerman, I., Wright, S., Takizawa, K., Henicke, B., Spielman, T., and Tezduyar, T., “3D simulation of wind turbine rotors at full scale. Part I: Geometry modeling and aerodynamics,” *International Journal for Numerical Methods in Fluids*, Vol. 65, (1-3), 2011, pp. 207–235.
- ³Potsdam, M. A. and Mavriplis, D. J., “Unstructured Mesh CFD Aerodynamic Analysis of the NREL Phase VI Rotor,” AIAA Paper 2009-1221, 47th AIAA Aerospace Sciences Meeting, Orlando, FL, January 2009.
- ⁴Sørensen, N. N., Michelsen, J., and Schreck, S., “Navier-Stokes predictions of the NREL phase VI rotor in the NASA Ames 80 ft × 120 ft wind tunnel,” *Wind Energy*, Vol. 5, (2-3), 2002, pp. 151–169.
- ⁵Duque, E. P., Burklund, M. D., and Johnson, W., “Navier-Stokes and comprehensive analysis performance predictions of the NREL phase VI experiment,” *Journal of Solar Energy Engineering*, Vol. 125, (4), 2003, pp. 457–467.
- ⁶Pape, A. L. and Lecanu, J., “3D Navier–Stokes computations of a stall-regulated wind turbine,” *Wind Energy*, Vol. 7, (4), 2004, pp. 309–324.
- ⁷Gomez-Iradi, S., Steijl, R., and Barakos, G., “Development and Validation of a CFD Technique for the Aerodynamic Analysis of HAWT,” *Journal of Solar Energy Engineering*, Vol. 131, (3), 2009, pp. 031009.
- ⁸Zahle, F., Sørensen, N. N., and Johansen, J., “Wind turbine rotor-tower interaction using an incompressible overset grid method,” *Wind Energy*, Vol. 12, (6), 2009, pp. 594–619.
- ⁹Bazilevs, Y., Hsu, M.-C., Kiendl, J., Wüchner, R., and Bletzinger, K.-U., “3D simulation of wind turbine rotors at full scale. Part II: Fluid–structure interaction modeling with composite blades,” *International Journal for Numerical Methods in Fluids*, Vol. 65, (1-3), 2011, pp. 236–253.
- ¹⁰Gundling, C., Roget, B., and Sitaraman, J., “Prediction of Wind Turbine Performance and Wake Losses using Analysis Methods of Incremental Complexity,” AIAA Paper 2011-458, 49th AIAA Aerospace Sciences Meeting, Orlando, FL, January 2011.
- ¹¹Gundling, C., Roget, B., Sitaraman, J., and Rai, R., “Comparison of Wind Turbine Wakes in Steady and Turbulent Inflow,” AIAA Paper 2012-899, 50th AIAA Aerospace Sciences Meeting, Nashville, TN, January 2012.
- ¹²Rai, R. K., Gopalan, H., Naughton, J. W., and Heinz, S., “A Study of the Sensitivity of Wind Turbine Response to Inflow Temporal and Spatial Scales,” , 2012.
- ¹³Li, Y., Paik, K.-J., Xing, T., and Carrica, P. M., “Dynamic overset CFD simulations of wind turbine aerodynamics,” *Renewable Energy*, Vol. 37, (1), 2012, pp. 285–298.
- ¹⁴Gopalan, H., Gundling, C., Brown, K., Roget, B., Sitaraman, J., Mirocha, J. D., and Miller, W. O., “A coupled mesoscale–microscale framework for wind resource estimation and farm aerodynamics,” *Journal of Wind Engineering and Industrial Aerodynamics*, Vol. 132, 2014, pp. 13–26.
- ¹⁵Hsu, M.-C., Akkerman, I., and Bazilevs, Y., “Finite element simulation of wind turbine aerodynamics: validation study using NREL Phase VI experiment,” *Wind Energy*, Vol. 17, (3), 2014, pp. 461–481.
- ¹⁶Scheurich, F. and Brown, R. E., “Modelling the aerodynamics of vertical-axis wind turbines in unsteady wind conditions,” *Wind Energy*, Vol. 16, (1), 2013, pp. 91–107.

- ¹⁷Gundling, C., Sitaraman, J., Roget, B., and Masarati, P., “Application and validation of incrementally complex models for wind turbine aerodynamics, isolated wind turbine in uniform inflow conditions,” *Wind Energy*, Vol. 18, (11), 2015, pp. 1893–1916.
- ¹⁸Wissink, A. M., Sitaraman, J., Sankaran, V., Mavriplis, D. J., and Pulliam, T. H., “A Multi-Code Python-Based Infrastructure for Overset CFD with Adaptive Cartesian Grids,” AIAA Paper 2008-927, 46th AIAA Aerospace Sciences Meeting, Reno, NV, January 2008.
- ¹⁹Solin, P., Segeth, K., and Dolezel, I., *Higher-order finite element methods*, CRC Press, 2003.
- ²⁰Burgess, N. K. and Mavriplis, D. J., “hp-Adaptive discontinuous Galerkin solver for the Navier-Stokes equations,” *AIAA Journal*, Vol. 50, (12), 2012, pp. 2682–2694.
- ²¹Brazell, M. J., Kirby, A. C., Sitaraman, J., and Mavriplis, D. J., “A Multi-Solver Overset Mesh Approach for 3D Mixed Element Variable Order Discretizations,” AIAA Paper 2016-2053, 54th AIAA Aerospace Sciences Meeting, San Diego, CA, January 2016.
- ²²Mavriplis, D. J., “Results from the 3rd Drag Prediction Workshop using the NSU3D Unstructured Mesh Solver,” AIAA Paper 2007-256, 45th AIAA Aerospace Sciences Meeting, Reno, NV, January 2007.
- ²³Mavriplis, D. and Pirzadeh, S., *Large-scale parallel unstructured mesh computations for 3D high-lift analysis*, American Institute of Aeronautics and Astronautics, 2015/06/01 1999.
doi: 10.2514/6.1999-537
- ²⁴Mavriplis, D. J., “Multigrid Strategies for Viscous Flow Solvers on Anisotropic Unstructured Meshes,” *Journal of Computational Physics*, Vol. 145, (1), 1998, pp. 141–165.
- ²⁵Long, M. and Mavriplis, D., “NSU3D Results for the First AIAA High Lift Prediction Workshop,” AIAA Paper 2011-0863, 49th AIAA Aerospace Sciences Meeting, Orlando, FL, January 2011.
- ²⁶Mavriplis, D. J., “Third Drag Prediction Workshop Results Using the NSU3D Unstructured Mesh Solver,” *Journal of Aircraft*, Vol. 45, (3), 2015/06/01 2008, pp. 750–761.
doi: 10.2514/1.29828
- ²⁷Brazell, M. J. and Mavriplis, D. J., “3D Mixed Element Discontinuous Galerkin with Shock Capturing,” AIAA Paper 2013-2855, 21st AIAA CFD Conference, San Diego, CA, June 2013.
- ²⁸Brazell, M. J. and Mavriplis, D. J., “High-Order Discontinuous Galerkin Mesh Resolved Turbulent Flow Simulations of a NACA 0012 Airfoil (Invited),” AIAA Paper 2015-1529, 53rd AIAA Aerospace Sciences Meeting, Kissimmee, FL, January 2015.
- ²⁹Kirby, A. C., Mavriplis, D. J., and Wissink, A. M., “An Adaptive Explicit 3D Discontinuous Galerkin Solver for Unsteady Problems,” AIAA Paper 2015-3046, 22nd AIAA Computational Fluid Dynamics Conference, Dallas, TX, June 2015.
- ³⁰Taylor, G. and Green, A., “Large Ones,” *Proceedings of the Royal Society of London. Series A, Mathematical and Physical Sciences*, Vol. 158, (895), 1937, pp. 499–521.
- ³¹Brachet, M., “Direct simulation of three-dimensional turbulence in the Taylor-Green vortex,” *Fluid Dynamics Research*, Vol. 8, (1), 1991, pp. 1–8.
- ³²Povitsky, A., “High-Incidence 3-D Lid-Driven Cavity Flow,” AIAA Paper 2001-2847, 15th AIAA Computational Fluid Dynamics Conference, Anaheim, CA, June 2001.
- ³³National Center for Atmospheric Research, Boulder, CO, *Yellowstone: IBM iDataPlex System (Climate Simulation Laboratory)*, <http://n2t.net/ark:/85065/d7wd3xhc>, 2012.
- ³⁴Hornung, R. D., Wissink, A. M., and Kohn, S. R., “Managing complex data and geometry in parallel structured AMR applications,” *Engineering with Computers*, Vol. 22, (3-4), 2006, pp. 181–195.
- ³⁵Gunney, B. T., Wissink, A. M., and Hysom, D. A., “Parallel clustering algorithms for structured AMR,” *Journal of Parallel and Distributed Computing*, Vol. 66, (11), 2006, pp. 1419–1430.
- ³⁶Kamkar, S., Jameson, A. J., and Wissink, A. M., “Automated Grid Refinement Using Feature Detection,” AIAA Paper 2009-1496, 47th AIAA Aerospace Sciences Conference, Orlando, FL, January 2009.
- ³⁷Roget, B. and Sitaraman, J., “Robust and efficient overset grid assembly for partitioned unstructured meshes,” *Journal of Computational Physics*, Vol. 260, 2014, pp. 1–24.
- ³⁸Brazell, M. J., Mavriplis, D. J., and Sitaraman, J., “An Overset Mesh Approach for 3D Mixed Element High Order Discretizations,” AIAA Paper 2015-1739, 53rd AIAA Aerospace Sciences Meeting, Kissimmee, FL, January 2014.
- ³⁹Hand, M. M., Simms, D., Fingersh, L., Jager, D., Cotrell, J., Schreck, S., and Larwood, S., *Unsteady aerodynamics experiment phase VI: wind tunnel test configurations and available data campaigns*, National Renewable Energy Laboratory, Golden, Colorado, USA, 2001.
- ⁴⁰Simms, D. A., Schreck, S., Hand, M., and Fingersh, L., *NREL unsteady aerodynamics experiment in the NASA-Ames wind tunnel: a comparison of predictions to measurements*, National Renewable Energy Laboratory Golden, CO, USA, 2001.
- ⁴¹Schreck, S., “The NREL full-scale wind tunnel experiment Introduction to the special issue,” *Wind Energy*, Vol. 5, (2-3), 2002, pp. 77–84.

⁴²Fingersh, L. J., Simms, D., Hand, M., Jager, D., Cotrell, J., Robinson, M., Schreck, S., and Larwood, S., “Wind Tunnel Testing of NRELs Unsteady Aerodynamics Experiment,” AIAA Paper 2001-35, 20th ASME Wind Energy Symposium and the 39th Aerospace Sciences Meeting, Reno, NV, 2001.

⁴³Sankaran, V., Sitaraman, J., Wissink, A., Datta, A., Jayaraman, B., Potsdam, M., Mavriplis, D., Yang, Z., OBrien, D., Saberi, H., *et al.*, “Application of the Helios Computational Platform to Rotorcraft Flowfields,” AIAA Paper 2010-1230, 48th AIAA Aerospace Meeting, Orlando, FL, 2010.

⁴⁴Wissink, A., Jayaraman, B., Datta, A., Sitaraman, J., Potsdam, M., Kamkar, S., Mavriplis, D., Yang, Z., Jain, R., Lim, J., *et al.*, “Capability Enhancements in Version 3 of the Helios High-Fidelity Rotorcraft Simulation Code,” AIAA Paper 2012-0713, 50th AIAA Aerospace Science Meeting, Nashville, TN, 2012.

⁴⁵Wissink, A. M., Kamkar, S., Pulliam, T. H., Sitaraman, J., and Sankaran, V., “Cartesian Adaptive Mesh Refinement for Rotorcraft Wake Resolution,” AIAA Paper 2010-4554, 28th Applied Aerodynamics Conference, Chicago, IL, 2010.

⁴⁶Sitaraman, J., Mavriplis, D., and Duque, E. P., “Wind farm simulations using a full rotor model for wind turbines,” Proceedings of the AIAA SciTech 2014 Meeting, National Harbor, MD, 2014.

⁴⁷Gundling, C. H., *Development and application of incrementally complex tools for wind turbine aerodynamics*, 2013.

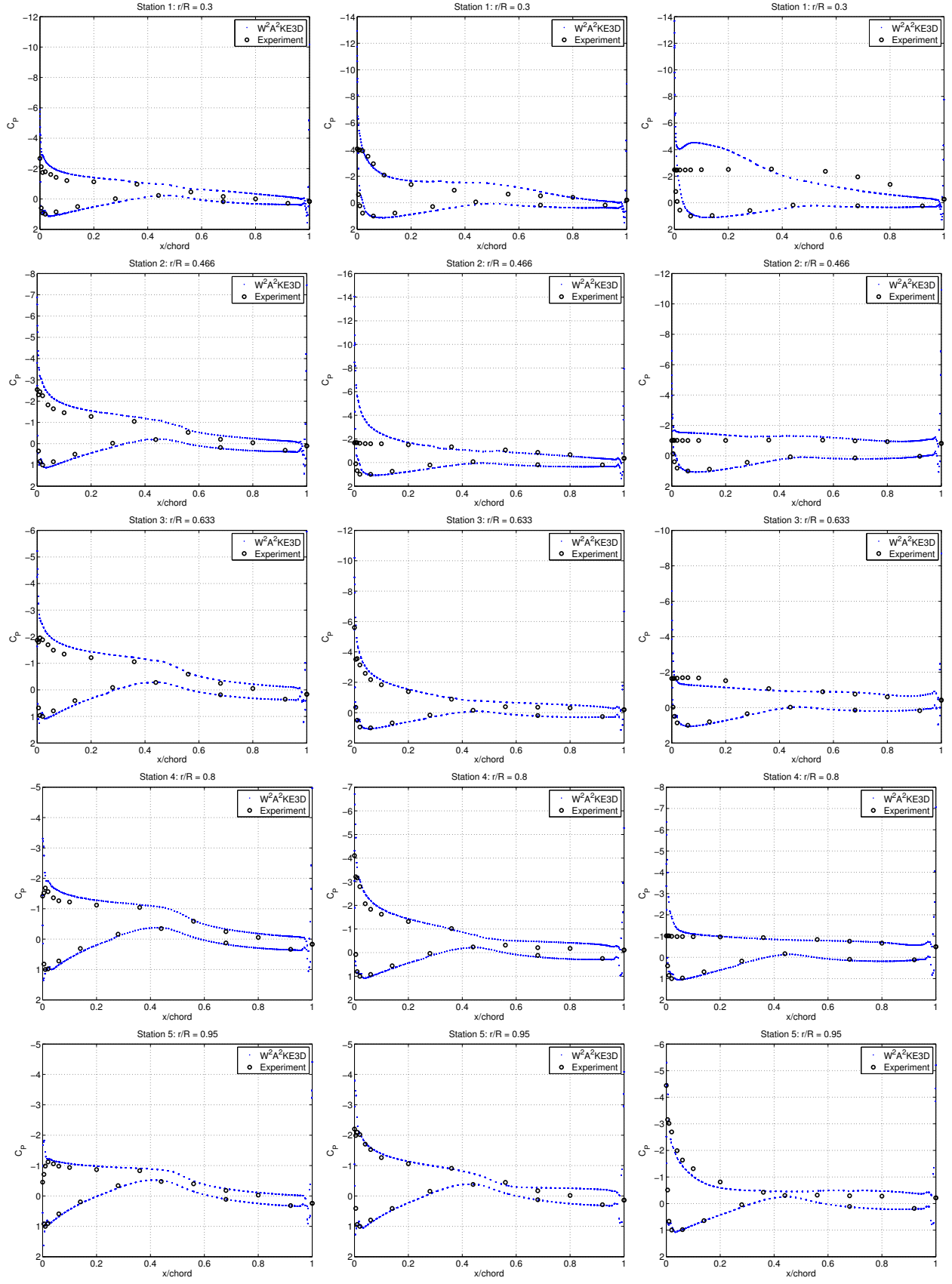


Fig. 8. Pressure coefficient at 30%, 46.6%, 63.3%, 80%, 95% spanwise stations for 7 m/s (column 1), 10 m/s (column 2), and 15 m/s (column 3) uniform axial inflow velocities using the smaller computational domain. Predicted results of W^2A^2KE3D are plotted versus the NREL experimental data.

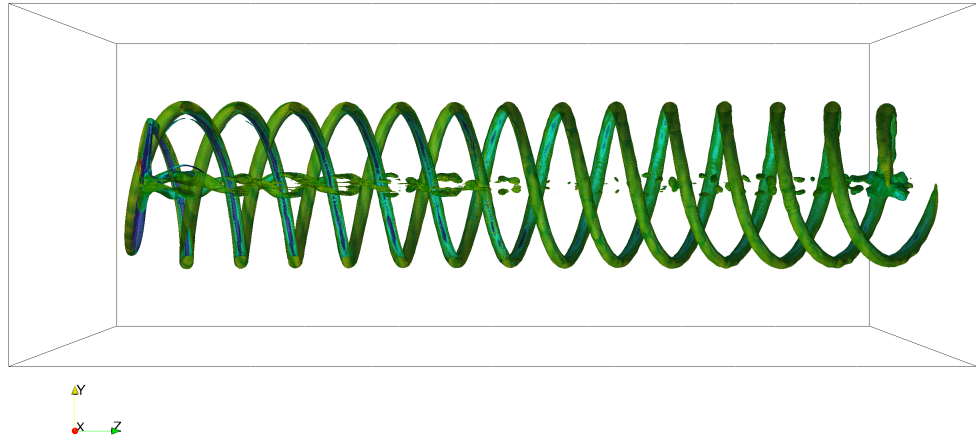


Fig. 9. Wind velocity contour of Phase VI wind turbine colored by density.

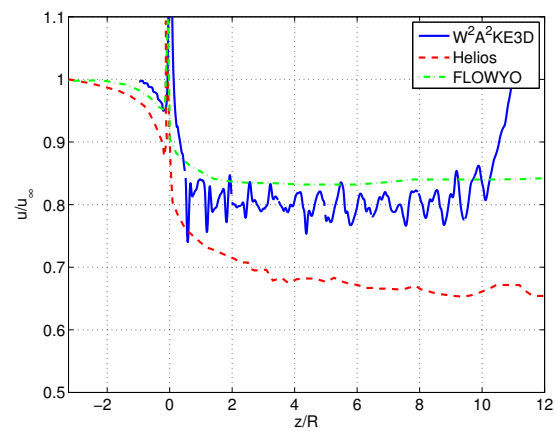


Fig. 10. Normalized wind velocity deficit along a line from the domain inlet to the domain outlet at a horizontal location of half the blade radius for inflow velocity of 10 m/s.

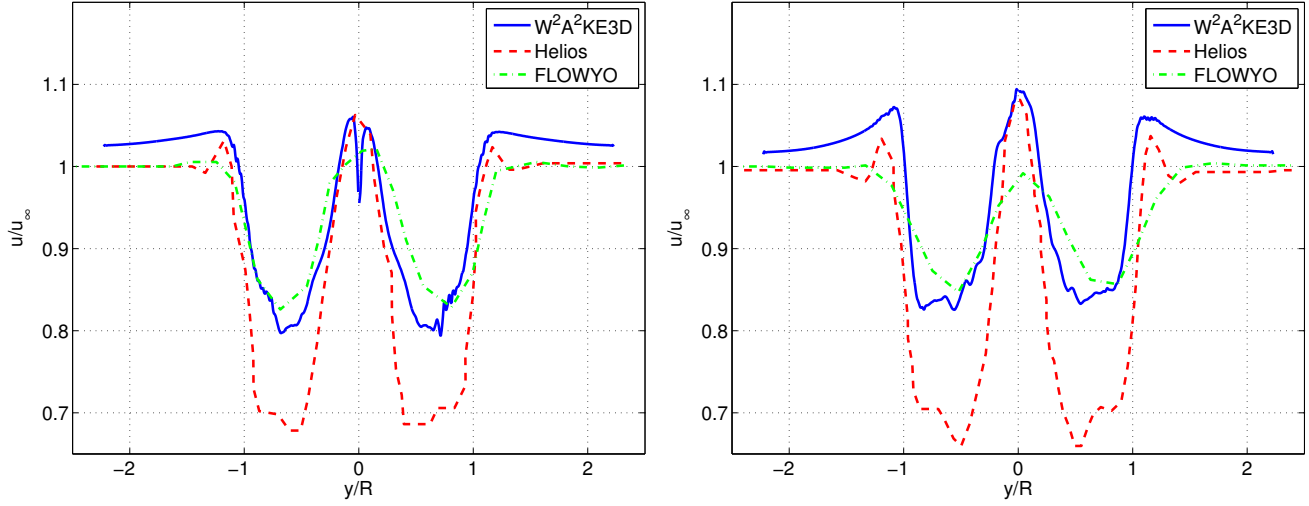


Fig. 11. Normalized wind velocity deficit for inflow velocity of 10 m/s at 5R (left) and 10R (right) lengths downstream of the turbine at a height of the center-line through the blade.

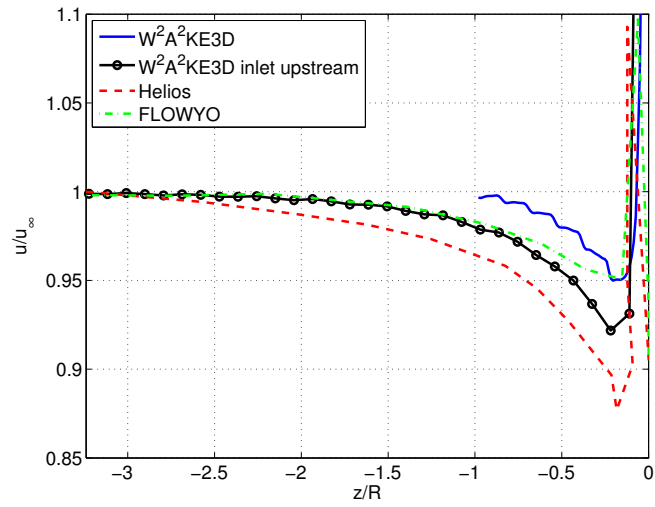


Fig. 12. Normalized wind velocity comparison along a line beginning at the inlet face to the rotor blade at a horizontal location of half the blade radius between the W^2A^2KE3D result using the initial domain Mesh-1 in Table 4, the W^2A^2KE3D result using the shifted domain Mesh-2 in Table 4, HELIOS, and FLOWYO.

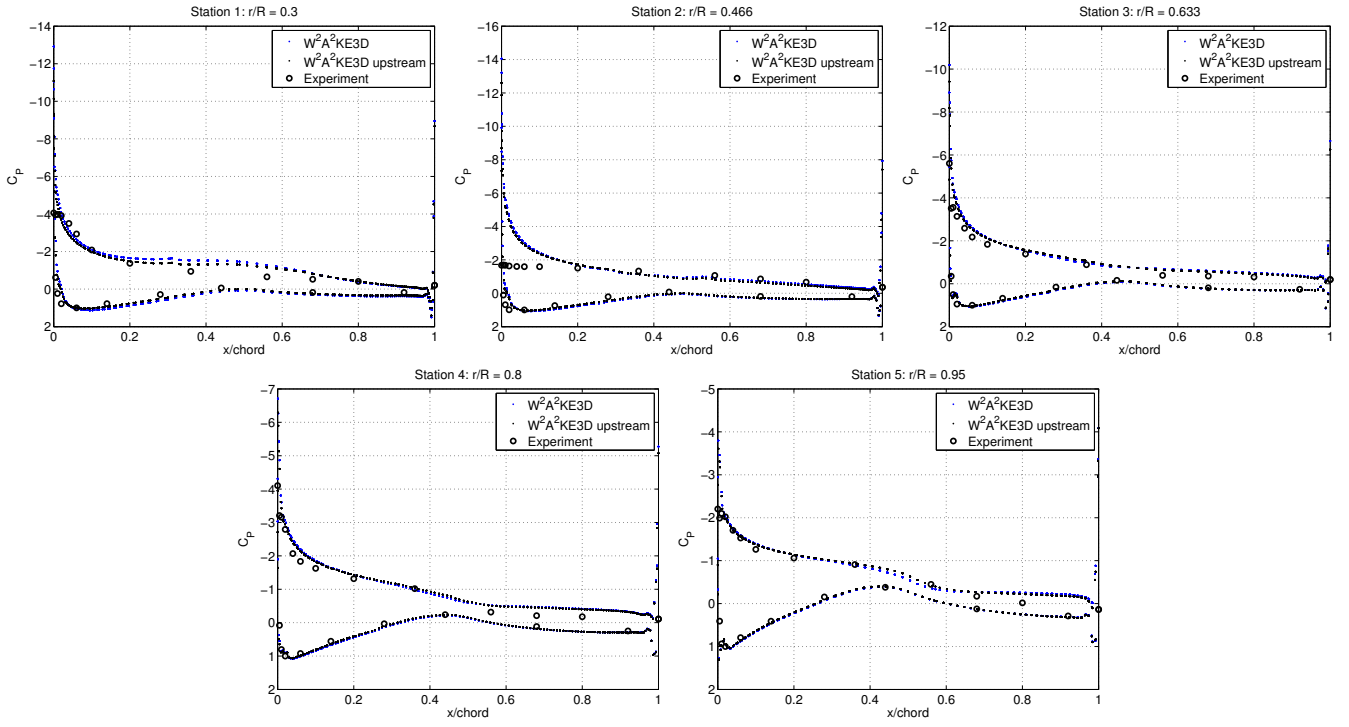


Fig. 13. Pressure coefficient comparisons at 30%, 46.6%, 63.3%, 80%, 95% spanwise stations for free-stream inflow velocities of 10 m/s using a smaller computational domain and a larger computational domain.

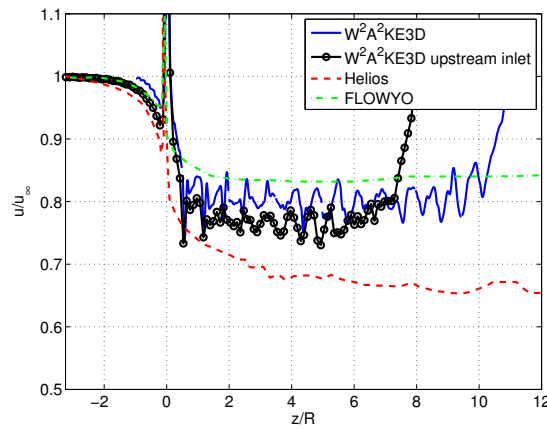


Fig. 14. Normalized wind velocity deficit along a line from the domain inlet to the domain outlet at a horizontal location of half the blade radius for inflow velocity of 10 m/s. The blue line is the solution using Mesh-1 from Table 4 and the black line with circle markers indicates the solution using Mesh-2 in Table 4.

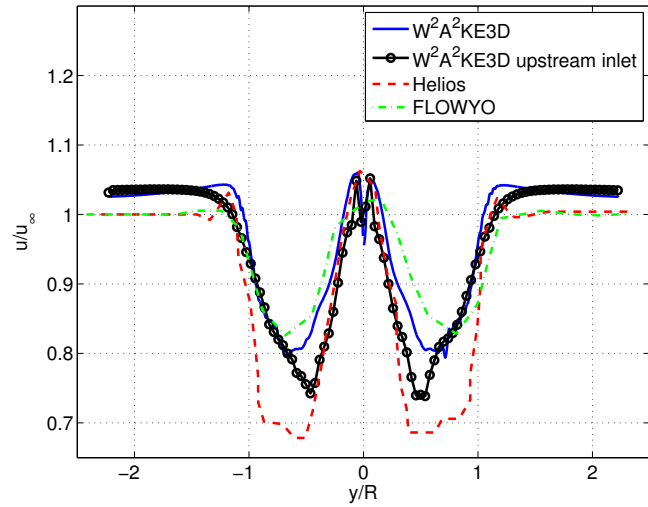


Fig. 15. Normalized wind velocity deficit for inflow velocity of 10 m/s at 5R (left) and 10R (right) lengths downstream of the turbine at a height of the center-line through the blade. The blue line is the solution using Mesh-1 from Table 4 and the black line with circle markers indicates the solution using Mesh-2 in Table 4.

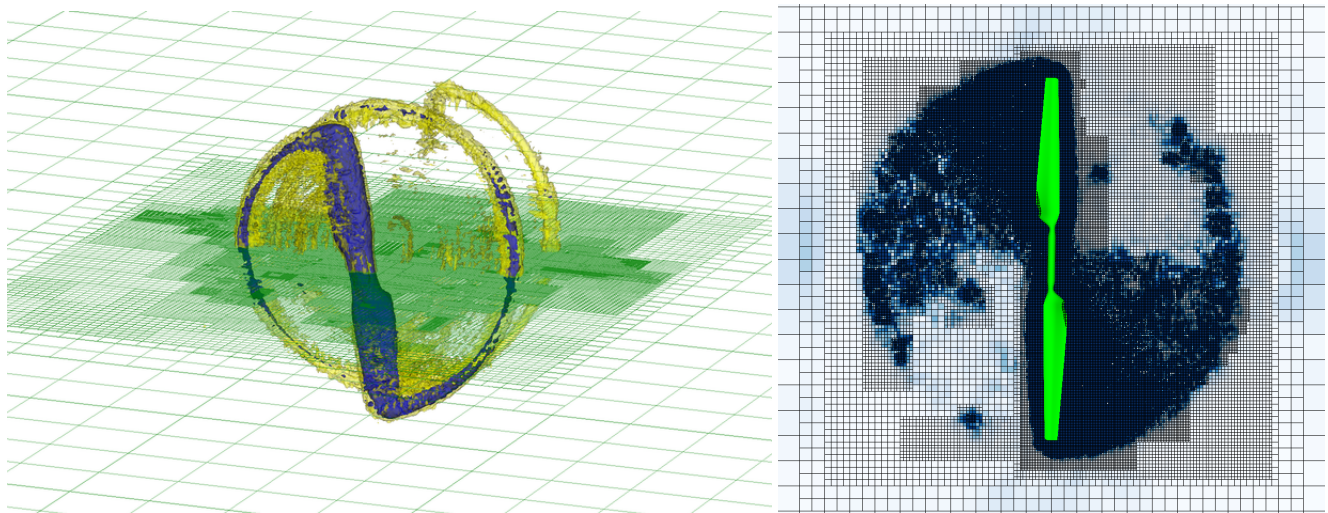


Fig. 16. Adaptive mesh solution using geometric and solution feature based adaption in SAMCartDG.